



Statistical discussions on skin frictional drag of turbulence over randomly distributed semi-spheres

メタデータ	言語: eng 出版者: 公開日: 2020-10-27 キーワード (Ja): キーワード (En): 作成者: Kuwata, Yusuke, Kawaguchi, Yasuo メールアドレス: 所属:
URL	http://hdl.handle.net/10466/00017114

Statistical discussions on skin frictional drag of turbulence over randomly distributed semi-spheres.

Yusuke Kuwata · Yasuo Kawaguchi

Received: date / Accepted: date

Abstract The influence of dynamical effects of rough wall turbulence, namely velocity dispersion, drag force and turbulence, on rough wall skin friction coefficient is statistically discussed by performing direct numerical simulation of rough-walled open channel flows and analyzing spatial and Reynolds (double) averaged equations. Numerical calculations are conducted by the D3Q27 multiple-relaxation-time lattice Boltzmann method (MRT-LBM). For the rough surfaces, randomly distributed semi-spheres are considered. Analyzing an integrated double averaged momentum equation, a main contributor to the skin friction coefficient is found to be the turbulence contribution and a second contributor is the drag contribution, and the drag contribution particularly increases with increasing the equivalent roughness. Although the streamwise mean velocity dispersion is significantly induced by the acceleration/deacceleration of the streamwise velocity due to the roughness elements, the wall-normal mean velocity dispersion is not significant. Consequently, the off-diagonal components of the dispersive covariant term is far smaller than the Reynolds shear stress and the velocity dispersion thus hardly contributes to an increase in the skin friction coefficient.

Keywords Rough wall turbulence · Direct numerical simulation · Volume averaging theory · Lattice Boltzmann method

Y. Kuwata
Osaka Prefecture University, 1-1 Sakai, Osaka, 599-8531, Japan
Tel.: +8172-254-6433
Fax: +8172-254-9904
E-mail: kuwata@me.osakafu-u.ac.jp

Y. Kawaguchi
Tokyo University of Science, 2641 Yamazaki, Noda, Chiba 278-8510

1 Introduction

Rough wall turbulence has historically attracted a great deal of attention because wall surfaces in most geophysical and engineering flows cannot usually be considered as hydraulically smooth. To say nothing of flows over vegetated, urban canopies and natural river beds, rough surfaces inevitably occur in engineering devices due to imperfections in the production processes, corrosion by aging, erosion or contamination. Those rough surfaces usually cause significant increase in turbulent frictional drag especially at high Reynolds number flows and prediction of the skin friction is thus crucial issue to design or maintain engineering devices. Since the pioneering work by [33] had demonstrated that the skin friction coefficient was a function of the equivalent sand grain in the fully rough regime, a large number of experimental studies have explored effective geometrical parameters of rough surfaces to determine the equivalent roughness [8, 10, 12, 14, 15, 31, 35, 37, 43, 44]. The proposed correlations were based on the shape parameter which accounted for the frontal area and the windward wetted surface area of a single roughness element [10, 37, 44] or statistical moments of surface elevation [14, 15, 31, 43]. The comprehensive reviews were given by [14]. Although many correlations have been proposed and extended with the help of the large number of experiments, the universal correlation toward prediction of the equivalent roughness has yet to be developed [14].

To develop universal correlation for the equivalent roughness, understanding underlying flow physics of rough wall turbulence is essentially required. Although most numerical attempts have been traditionally limited to ordered arrangement of roughness elements or two-dimensional structures, the modern computer technology enables us to perform direct numerical simulation (DNS) of irregular or scanned rough surfaces [4, 5, 32], which can provide detailed information of the drag force, the mean velocity dispersion and turbulence within real rough surfaces. However, as far as the authors know, the influence of those dynamical effects on the skin friction coefficient has not been studied.

Accordingly, this study statistically discusses the dynamical effects based on the double (spatial and Reynolds) averaging theory and aims to reveal the influence of those effects such as the drag force, the mean velocity dispersion and turbulence on the skin friction coefficient by performing DNS of turbulence over randomly distributed semi-spheres.

2 Numerical scheme

Owing to the simplicity of wall treatment for the curved boundary, the lattice Boltzmann method (LBM) achieved considerable success in complex flow simulations [1, 7, 34, 39, 40]. In particular, since the LBM algorithm inheres high spatial and temporal locality, the LBM is ideal in massive parallel computing using the MPI and GPUs [19, 30]. Additionally, the nature of the low numerical dissipation and dispersion leads to success in DNS of fundamental turbulent flows [6, 13, 17, 29, 38, 45]. The above mentioned advantages enable us to apply

the LBM to various complex turbulent flow problems such as flows around porous [18, 25, 27, 28] or over rough walls [21, 41].

The lattice Boltzmann equation can be obtained by discretizing the velocity space of the Boltzmann equation into a finite number of discrete velocity $\xi_\alpha \{\alpha = 0, \dots, Q - 1\}$. There are several discrete velocity models for three-dimensional flow simulations such as the D3Q15, D3Q19 and D3Q27 models. It was reported that although unphysical spurious currents were sometimes visible in the D3Q15 and D3Q19 models in axisymmetric flows, they were effectively suppressed by the D3Q27 model [22, 24, 46]. Also, to ensure the numerical stability for high Reynolds number flow simulations, it is effective to apply the multiple-relaxation-time (MRT) scheme for the collision process [9]. Accordingly, the present study employs the D3Q27 MRT-LBM [38]. The time evolution of the distribution function of the MRT-LBM can be written as

$$\begin{aligned} & | \mathbf{f}(\mathbf{x} + \xi_\alpha \delta t, t + \delta t) \rangle - | \mathbf{f}(\mathbf{x}, t) \rangle \\ &= -\mathbf{M}^{-1} \hat{\mathbf{S}} [| \mathbf{m}(\mathbf{x}, t) \rangle - | \mathbf{m}^{eq}(\mathbf{x}, t) \rangle], \end{aligned} \quad (1)$$

where the notations such as $|\mathbf{f}\rangle$ is $|\mathbf{f}\rangle = (f_0, f_1, \dots, f_{26})^T$ and δt denotes the time step and ξ_α represents the discrete velocity vector. The matrix \mathbf{M} is a 27×27 matrix which linearly transforms the distribution functions to the moments $|\mathbf{m}\rangle = \mathbf{M}|\mathbf{f}\rangle$. The collision matrix $\hat{\mathbf{S}}$ is diagonal;

$$\begin{aligned} \hat{\mathbf{S}} \equiv & \text{diag}(0, 0, 0, 0, s_4, s_5, s_5, s_7, s_7, s_7, s_7, s_{10}, s_{10}, s_{10}, s_{10}, \\ & s_{13}, s_{13}, s_{13}, s_{16}, s_{17}, s_{18}, s_{18}, s_{20}, s_{20}, s_{20}, s_{20}, s_{23}, s_{23}, s_{23}, s_{26}). \end{aligned} \quad (2)$$

The relaxation parameters are

$$\begin{aligned} s_4 &= 1.54, \quad s_5 = s_7, \quad s_{10} = 1.5, \quad s_{13} = 1.83, \quad s_{16} = 1.4, \\ s_{17} &= 1.61, \quad s_{18} = s_{20} = 1.98, \quad s_{23} = s_{26} = 1.74. \end{aligned} \quad (3)$$

The relaxation parameters s_5, s_7 are related to the kinematic viscosity ν ,

$$\nu = c_s^2 \left(\frac{1}{s_5} - \frac{1}{2} \right) \delta t = c_s^2 \left(\frac{1}{s_7} - \frac{1}{2} \right) \delta t. \quad (4)$$

The equilibrium moments, transformation and collision matrixes presently employed are as in [38]. The sound speed $c_s = 1/\sqrt{3}c$ with $c = \Delta/\delta t$ and Δ is the lattice spacing. Through the rigorous validation in the turbulent channel flows at friction Reynolds number of 180, it was confirmed by [38] that the higher order turbulence statistics including the budget terms in the transport equation of the turbulent kinetic energy agreed well with those obtained by the spectrum method.

3 Flow conditions

This study performs DNS of turbulent rough-walled open channel flows at friction Reynolds number 300 as illustrated in Figure 1. A slip boundary is considered to the top boundary surface whilst the rough wall is considered for the bottom wall. Periodic boundary conditions are applied to the streamwise and spanwise boundary faces with a constant streamwise pressure difference. To impose non-slip boundary conditions to rough surfaces keeping the second order spatial accuracy, a linear interpolated bounce-back scheme [2] is used. The computational domain size $L_x(x) \times L_y(y) \times L_z(z)$ corresponds to $6\delta(x) \times \delta(y) \times 3\delta(z)$, which is carefully validated by comparing the turbulence statistics with those obtained in twice larger domain simulation. Here, δ denotes the half channel height. The grid block of $1201(x) \times 70(y) \times 601(z)$ whose resolution corresponds to 1.5 wall units is set around the rough wall region of $y/\delta < 0.35$ while the twice coarser grid of $601(x) \times 66(y) \times 301(z)$ covers the other clear fluid region. The grid resolution in the present DNS is comparable to the other previous LBM-DNS studies [17, 27, 28, 38]. The distribution function between the fine and coarse grids is exchanged by using a method of [11] with an imbalance correction [26], which can successfully remove the momentum and mass conservation imbalances. The grid independence is confirmed after comparing the turbulence statistics with those obtained by the simulation with 1.5 times denser mesh.

The averaged friction velocity of the rough surface: u_τ is computed by the balance between the pressure drop: ΔP and the averaged wall shear stress of the rough wall: $\tau_w = \rho u_\tau^2$ as

$$S_{in}\Delta P = L_x L_z \tau_w, \quad (5)$$

where S_{in} is the inlet boundary surface area of fluid phase which can be surrogated as $S_{in} \approx L_z \delta^*$. Here, effective half channel height is defined as $\delta^* = \int_0^\delta \varphi dy$. Thus, u_τ is given as

$$u_\tau = \left(\frac{\Delta P}{\rho} \frac{\delta^*}{L_x} \right)^{0.5}. \quad (6)$$

In the following discussions, the value with the superscript “ $()^+$ ” indicates the value normalised by the friction velocity at the rough wall u_τ .

4 Rough walls

The rough walls considered in the present study are generated by randomly packing various size of semi-spheres to a smooth solid wall. The semi-sphere diameters are determined satisfying the probability density function $f(D)$ based on the Gaussian distribution:

$$f(D) = \frac{1}{\sqrt{2\pi}\sigma} \exp\left(-\frac{(D-\mu)^2}{2\sigma^2}\right), \quad (7)$$

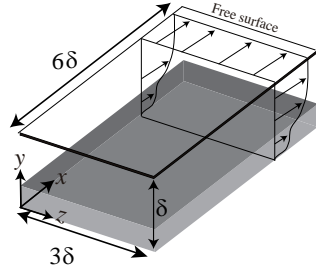


Fig. 1 Computational geometry of rough walled open channel flows.

where D , μ and σ are the semi-sphere diameter, a mean value and a standard deviation. To generate the semi-sphere diameters satisfying the PDF of Eq.(3), the Box-Muller's method [3] is used as

$$D = \sigma \sqrt{-2\log(r_{a1})} \cos(2\pi r_{a2}) + \mu, \quad (8)$$

where r_{a1} and r_{a2} are the random numbers: $r_{a1}, r_{a2} \in (-1, 1)$. The generated semi-spheres are randomly packed to a smooth solid wall allowing meddling among semi-spheres. Changing the number of the semi-spheres: N_s and σ keeping μ to be constant, three rough walls of the different equivalent roughness as depicted in Fig.2 are generated. The controlling parameters (N_s , σ and μ) and statistical moments of the roughness height profile such as the mean height: h_m , the standard deviation: h_{rms} and the skewness: Sk defined as

$$h_m = \frac{1}{A} \int_s h ds, \quad (9)$$

$$h_{rms} = \left(\frac{1}{A} \int_s (h - h_m)^2 ds \right)^{1/2}, \quad (10)$$

$$Sk = \frac{1}{Ah_{rms}^3} \int_s (h - h_m)^3 ds, \quad (11)$$

are listed in Table 1. Here, h represents rough surface height from the bottom solid wall and S denotes the bottom solid wall before adding on roughness. The area of S is expressed as A . The resultant skin friction coefficient: $C_f = \tau_w / (0.5\rho U_b^2)$ and surrogated the equivalent roughness: k_s are also listed in Table 1. Note that k_s is surrogated to collapse the computed roughness function to the empirical correlation between the roughness function and the equivalent roughness in the transitionally rough regimes [33]. Here, the bulk mean velocity is defined as $U_b = Q / (L_z \delta^*)$ where Q denotes the mean flow rate.

It can be seen in Table 1 that the skin friction coefficient increases in order of cases I, II and III. This means that the influence of the rough wall, which is quantified by the inner-normalized equivalent roughness, increases in this order. Judging from the approximate by [33], turbulence over the rough wall

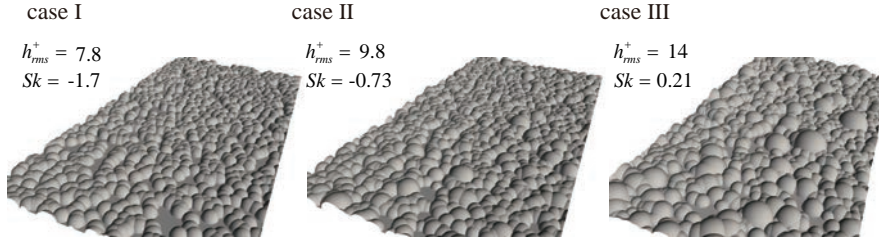


Fig. 2 Simulated randomly distributed semi-sphere rough surfaces

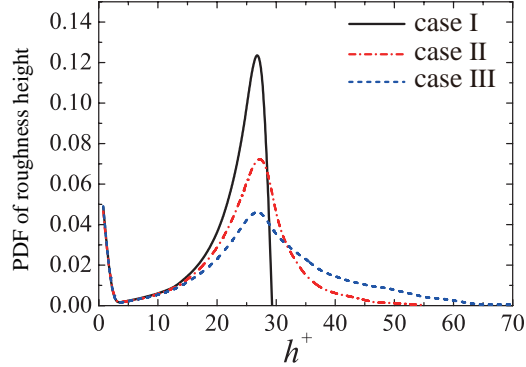


Fig. 3 Probability density function of rough surface height.

Table 1 Characteristics parameters of the simulated rough walls.

case	μ/δ	σ/μ	N_s	h_m/δ	h_{rms}^+	Sk	C_f	k_s^+
I	0.2	0.00	1,650	0.072	7.8	-1.7	0.0097	18
II	0.2	0.17	1,600	0.079	9.8	-0.73	0.0139	35
III	0.2	0.33	1,450	0.094	14	0.21	0.0205	70

in cases I and II corresponds to the transitionally rough regimes whereas the equivalent roughness in case III is computed as $k_s^+ = 70$ which corresponds to the onset of the fully rough regimes. To see the characteristics of the generated rough surfaces, the probability density function of the surface height profile is shown in Figure 3. It is observed that the roughness of $h^+ \approx 25$ mostly occupies the rough wall in all cases. However, the probability density of the surface height of $h^+ > 30$ suddenly decreases in case I whereas higher roughness elements increasingly exist in cases II and III. This means that the rough wall in case I is dominated by the valley which is reflected by the negative Sk . On the hand, in case III, the maximum roughness height reaches $h^+ \approx 80$ despite the fact that the probability density function still has a peak at $h^+ \approx 25$, which indicates the presence of the higher and isolated roughness elements in case III. The peak-dominated characteristics in case III is reflected by the positive Sk as seen in Table 1.

5 Results and Discussions

To discuss turbulence statistics around rough walls, double (Reynolds and plane) averaging operations are applied. The $x-z$ plane intrinsic (fluid phase) averaging for a variable ϕ is introduced as

$$\langle \phi \rangle^f(y) = \frac{1}{A_{S_f}} \int_S \phi(x, y, z) dS, \quad (12)$$

where S and A_{S_f} denote the $x-z$ plane and the plane areas of the fluid phase contained within S , respectively. The superficial averaging is also introduced as

$$\langle \phi \rangle(y) = \frac{1}{A_S} \int_S \phi(x, y, z) dS, \quad (13)$$

where A_S denotes the surface areas of $x-z$ plane. Between them the relation: $\langle \phi \rangle = \varphi \langle \phi \rangle^f$, exists with the plane porosity: $\varphi = A_{S_f}/A_S$. A variable ϕ can be decomposed into contribution from an intrinsic averaged value: $\langle \phi \rangle^f$ and deviation from the intrinsic averaged value (dispersion): $\tilde{\phi}$ as

$$\phi = \langle \phi \rangle^f + \tilde{\phi}. \quad (14)$$

To discuss the time dependent flows, the Reynolds decomposition: $\phi = \bar{\phi} + \phi'$ is also introduced. Here, $\bar{\phi}$ denotes the Reynolds averaged value and ϕ' denotes the fluctuation in time. To obtain the statistics, numerical calculation is carried over 100 cycle time after the flows have reached the fully developed states.

Applying the Reynolds and plane averaging to the Navier-Stokes equation, the double averaged momentum equation for incompressible flows can be derived as

$$\begin{aligned} \frac{D\langle \bar{u}_i \rangle^f}{Dt} &= -\frac{1}{\rho} \frac{\partial \langle \bar{p} \rangle^f}{\partial x_i} + \frac{1}{\varphi} \frac{\partial}{\partial x_k} \left(\nu \frac{\partial \varphi \langle \bar{u}_i \rangle^f}{\partial x_k} \right) \\ &\quad - \frac{1}{\varphi} \frac{\partial}{\partial x_k} \left(\underbrace{\varphi \langle \tilde{u}_i \tilde{u}_k \rangle^f}_{\mathcal{T}_{ik}} + \underbrace{\varphi \langle u'_i u'_k \rangle^f}_{R_{ik}} \right) - \underbrace{\frac{\nu}{\varphi} \frac{\partial \varphi}{\partial x_k} \frac{\partial \langle \bar{u}_i \rangle^f}{\partial x_k}}_{g_i} \\ &\quad - \underbrace{\left(\frac{1}{\rho A_{S_f}} \int_L \tilde{p} n_i d\ell - \frac{\nu}{A_{S_f}} \int_L n_k \frac{\partial \tilde{u}_i}{\partial x_k} d\ell \right)}_{f_i}, \end{aligned} \quad (15)$$

where L represents obstacle perimeter within an averaging plane, ℓ represents circumference length of solid obstacles and n_k is its unit normal vector pointing outward from the fluid to the solid phase.

The second moment terms $\mathcal{T}_{ij} = \varphi \langle \tilde{u}_i \tilde{u}_j \rangle^f$ and $R_{ij} = \varphi \langle u'_i u'_j \rangle^f$ are the plane-dispersive covariance and the plane-averaged Reynolds stress, respectively. The inhomogeneous correction term g_i arises due to the inhomogeneity of the plane porosity φ , and f_i is the drag force term consisting of the surface integration of the viscous stress dispersion and the pressure dispersion representing the viscous and form drag effects.

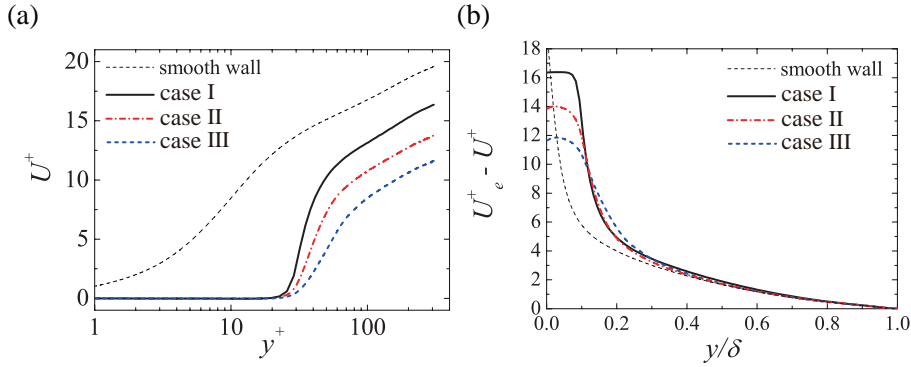


Fig. 4 Streamwise mean velocity profiles: (a) with semi-logarithmic wall scaling, (b) with velocity defect forms.

5.1 Mean velocity

Figure 4 (a) and (b) respectively shows the $x - z$ plane superficial averaged streamwise mean velocity profiles $U^+ = \varphi \langle \overline{u^+} \rangle^f$ with semi logarithmic scaling and defect form. For comparison, a profile of smooth wall case at friction Reynolds number of 300 [20] is also plotted. As shown in Fig. 4 (a), owing to the presence of the wall roughness, U^+ is almost damped to zero inside rough wall of $y^+ < 20$. The increase in the skin friction as seen in Table 1 makes the profile of U^+ over the rough wall shift downward displaying the slope of the linear log-law profile in outer layer. To examine U^+ profiles in the outer layer region, profiles of U^+ are presented in the defect form $U_e^+ - U^+$ in Fig.4(b). Here, U_e^+ denotes U^+ at the slip wall of $y/\delta = 1$. All profiles including rough and smooth wall cases almost overlap in the region of $y/\delta > 0.4$, which indicates that the influence of the wall roughness is confined near the rough wall region. This fact supports the idea of outer layer similarity of [42] and the present result is consistent with the many other studies on rough wall turbulence [23, 36].

5.2 Turbulence and dispersion intensities

Figure 5 gives the $x - z$ plane superficial averaged turbulent intensities: $\varphi \sqrt{\langle \overline{u'_i u'_j} \rangle^f}$. Also shown for comparison are results of the smooth wall case, and a position of the roughness peak is also shown. All profiles are almost consistent outside the rough wall region of $y/\delta > 0.3$ while a clear discrepancy can be seen around the rough wall region, which implies that the influence of the wall roughness is confined around the rough walls and this observation is consistent with the mean velocity profiles in Fig. 4. Although the wall roughness significantly damps the turbulent intensities in the region of $0.1 < y/\delta < 0.2$, the turbulent intensities are not decayed to zero even deeply inside the rough wall of

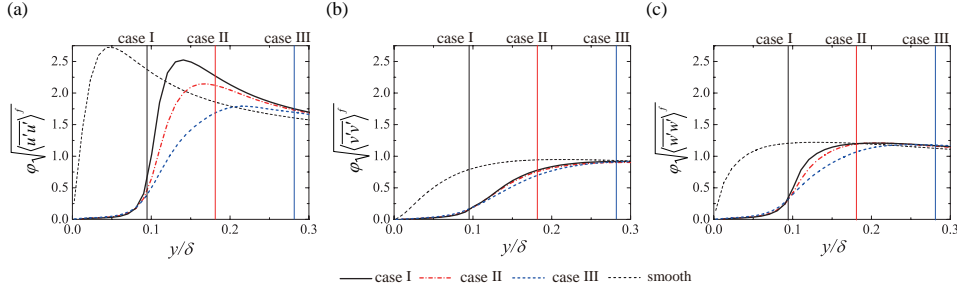


Fig. 5 Plane-averaged turbulent intensities: (a) streamwise component, (b) wall-normal component, (c) spanwise component.

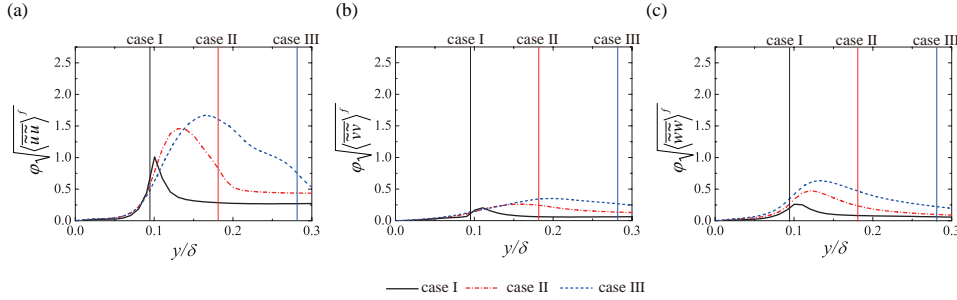


Fig. 6 Plane-dispersion intensities: (a) streamwise component, (b) wall-normal component, (c) spanwise component.

$y/\delta < 0.1$ despite the fact that the streamwise mean velocity is completely damped by the wall roughness as seen in Fig.4. Additionally, the profiles of the turbulent intensities in all cases are found to collapse well in the region of $y/\delta < 0.1$. This suggests that turbulence can penetrate deeply inside the rough wall to the same extent irrespective of the difference of the presently tested rough surfaces. As shown in Fig.5(b) and (c), it is observed that the difference of the equivalent roughness does not significantly affect the wall-normal component even around the rough walls while maximum peak of the streamwise component considerably decreases with increasing the equivalent roughness. This implies that the reduction of the streamwise turbulent fluctuation due to the wall roughness depends strongly on the equivalent roughness while the wall-normal turbulence fluctuation does not.

Owing to the spatial inhomogeneity of the rough surfaces, there exists the mean velocity dispersion. To examine the magnitude of the mean velocity dispersion, the plane-dispersion intensity: $\varphi \sqrt{\langle \overline{\tilde{u}_i \tilde{u}_j} \rangle}$ is compared in Figure 6. The streamwise and wall-normal mean velocity dispersion distribution in the $x-y$ and $x-z$ planes in case III are respectively visualized in Figures 7 and 8. In Fig.6, the plane-dispersion intensity increases with increasing the equivalent roughness and the plane-dispersion induced by the roughness is found to remain even away from the rough wall in all cases. In particular, as the equivalent

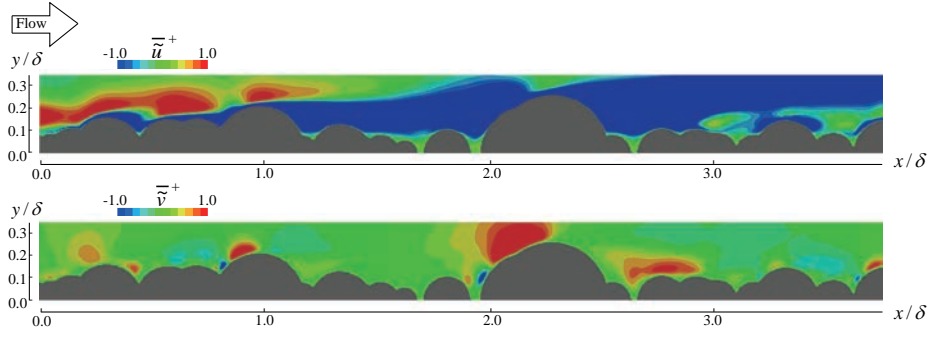


Fig. 7 Mean dispersion velocity distributions in a $x - y$ plane in case III: (a) streamwise component, (b) wall-normal component.

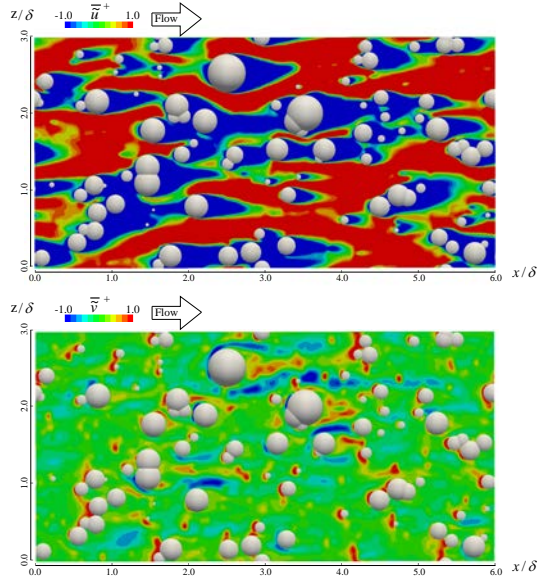


Fig. 8 Mean dispersion velocity distributions in a $x - z$ plane at a position of a mean roughness height $y = h_m$ in case III: (a) streamwise component, (b) wall-normal component.

roughness increases, the streamwise plane-dispersion intensity is increasingly generated and the level of the streamwise dispersion intensity in case III becomes comparable to the streamwise turbulent intensity within the rough wall region of $y/\delta < 0.2$. Although the wall-normal turbulent intensity in Fig. 5(b) is not influenced by the difference of the equivalent roughness, the wall-normal plane-dispersion intensity increases with increasing the equivalent roughness. The wall-normal mean velocity dispersion is induced by upward/downward fluid motions observed near the roughness peak as shown in Fig. 7, while the streamwise mean velocity dispersion appears to be induced by the acceleration/deceleration of the streamwise velocity due to the roughness elements.

The acceleration effects inducing the positive velocity dispersion is caused by the contraction of the fluid phase area due to the presence of the obstacles whereas the deacceleration inducing the negative velocity dispersion is caused due to the drag force by the roughness. It is observed from 8 that the generation of the wall-normal velocity dispersion is confined vicinity of the roughness elements whereas the streamwise velocity dispersion distributes over a wide region.

5.3 Momentum transfer

The diagonal component of the second moments (shear stresses) of \mathcal{T}_{12} and R_{12} are depicted in Fig.9. As the equivalent roughness increases, the plane-averaged Reynolds shear is more damped resulting primarily from the reduction of the streamwise turbulent intensity around the rough wall as seen in Fig.5(a). Although the streamwise and wall-normal dispersion intensities become significant over the roughness peak in case I as shown in Fig.6(a) and (b), \mathcal{T}_{12}^+ in case I is negligibly small, which implies weak coherence between the streamwise and wall-normal dispersion velocity in case I. The plane-dispersive covariance \mathcal{T}_{12} in case III, in contrast, exhibits meaningful values near $y/\delta \sim 0.15$ where the streamwise dispersion intensity reaches the maximum.

Figure 10 presents the streamwise plane-averaged drag force f_x and the inhomogeneous correction g_x normalized by U_b and δ . Clearly, the plane-averaged drag force term is found to surpass the inhomogeneous correction term in all cases. The terms f_x and g_x in case I exhibit the pointed peak just below the roughness peak while the maximum peak values of f_x and g_x decrease with increasing the equivalent roughness. Interestingly, it is found that the profiles of f_x and g_x are similar to the profile of the probability density function of the roughness peak as shown in Fig.3, this means that the influence of f_x and g_x may be well characterized by the probability density function. This observation may support the fact that the characteristic parameters related to the probability density function of the rough surface elevation, namely the h_{rms} and Sk , can reasonably represent the increase in the skin frictional drag of rough wall turbulence.

5.4 Skin friction coefficient

Finally, the contribution of the dynamical effects to the skin friction coefficient is discussed. Applying triple integration over the wall-normal direction to Eq.(15) with normalization of δ and $2U_b$, the FIK identity [16] for the plane and Reynolds averaged system can be derived as

$$C_f = \frac{1}{C_{FIK}} \left(\underbrace{\frac{4}{Re_b}}_{laminar} + \underbrace{8 \int_0^1 (1-y)(-R_{12}) dy}_{turbulence} + \underbrace{8 \int_0^1 (1-y)(-\mathcal{T}_{12}) dy}_{dispersion} \right)$$

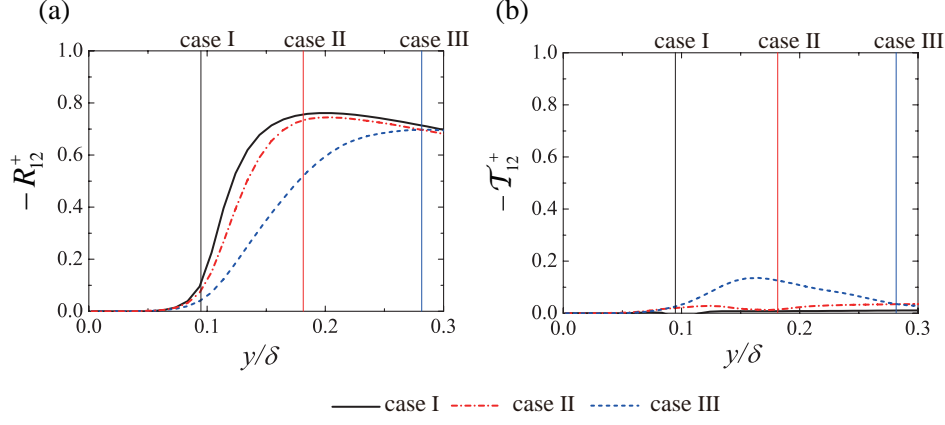


Fig. 9 Shear stress profiles: (a) plane-averaged Reynolds shear stress, (b) plane-dispersive covariance.

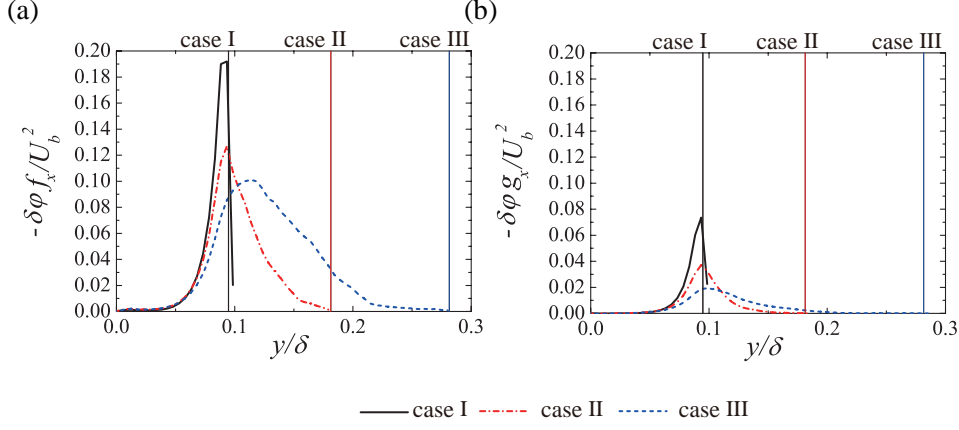


Fig. 10 The additional terms in the double averaged momentum equation: (a) plane-averaged drag force term, (b) inhomogeneous correction term.

$$\left. \underbrace{+8 \int_0^1 \left(y - \frac{1}{2}y^2 \right) (\varphi f_x) dy}_{\text{drag}} + \underbrace{+8 \int_0^1 \left(y - \frac{1}{2}y^2 \right) (\varphi g_x) dy}_{\text{inhomogeneous correction}} \right), \quad (16)$$

where Re_b is the bulk mean Reynolds number, and C_{FIK} is expressed as

$$C_{FIK} = \frac{\delta}{\delta^*} \int_0^1 \left(y - \frac{1}{2}y^2 \right) \varphi dy. \quad (17)$$

Note that the all dimensional values in Eq. (16) are normalized by δ and $2U_b$. The dispersion, drag and inhomogeneous correction contribution appear as

well as the laminar and turbulence contributions. The dispersion contribution is expressed as the integration of the weighted dispersive covariance: $(1 - y)\mathcal{T}_{12}$, which means that \mathcal{T}_{12} near the wall more contributes to the skin friction coefficient. It is interesting to note that, unlike R_{12} and \mathcal{T}_{12} , the weighting function for f_x and g_x : $(y - \frac{1}{2}y^2)$ increases with increasing the distance from the wall. Hence, this suggests that f_x and g_x away from the wall more contribute to the skin friction coefficient.

Figure 11 shows the contribution to the skin friction coefficient. It is revealed that the most dominant contribution to C_f is turbulence and second contribution is found to be the drag. The turbulence and drag contributions increase with increasing the equivalent roughness. In particular, the increasing in the drag contribution is more remarkable despite the fact that maximum peak value of f_x decreases with increasing the equivalent roughness as seen in Fig.10. This can be attributed to the weighting function for f_x . Although the maximum peak of f_x in case III is lower than that in case I, \bar{f}_x away from the bottom wall is increasingly generated due to the presence of the higher roughness as shown in Fig.10(a) whose contribution to C_f is more enhanced by the weighting function: $(y - \frac{1}{2}y^2)$. The laminar and inhomogeneous correction contributions are almost constant independent of the equivalent roughness. The influence of the dispersion slightly appears in case II and III, however, the contribution is 3% at most in case III.

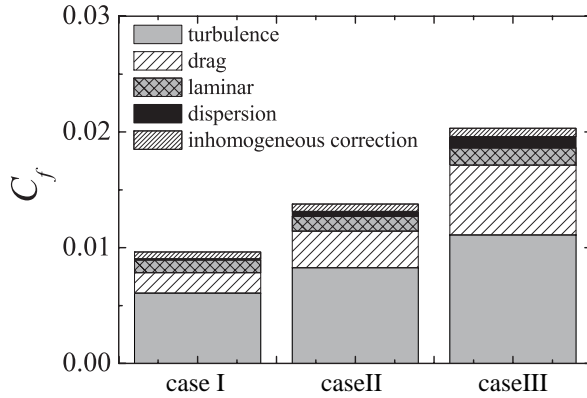


Fig. 11 Contribution to the skin friction coefficient.

6 Conclusion

This study statistically discusses the influence of the dynamical effects of rough wall turbulence, namely velocity dispersion, drag force and turbulence, on skin friction coefficient by analyzing the spatial and Reynolds averaged equation using the DNS results. The direct numerical simulation of turbulence over

randomly distributed semi-sphere at friction Reynolds number of 310 is conducted by the D3Q27 multiple-relaxation-time lattice Boltzmann method with the grid refinement technique. Analyzing an integrated spatial and Reynolds averaged momentum equation, it is revealed that a main contributor to the skin friction coefficient is turbulence contribution and a second contributor is drag contribution, and those contributions increase with increasing the equivalent roughness. It is found that since the drag contribution to the skin friction coefficient is expressed as the weighted integration of the drag force whose weighted function increase as increase the distance from the bottom wall, the drag force away from the bottom wall more contribute to the skin friction coefficient. Indeed, the drag force generated by higher roughness significantly contributes to the increase of the skin friction coefficient. The streamwise mean velocity dispersion is found to be induced by the acceleration/deacceleration of the streamwise velocity due to the roughness elements. However, since the wall-normal mean velocity dispersion is not significant, the covariant terms of the mean velocity dispersion is found to be far smaller than the plane-averaged Reynolds shear stress. Therefore, velocity dispersion contribution to the skin friction coefficient is marginal compared with the turbulence and drag contributions.

Acknowledgements The authors express their gratitude to their colleagues: PhD. K. Suga, Dr. M. Kaneda and Dr. T. Tsukahara for their supports. A part of this study was financially supported by the research grants (No.17K14591, 16K14162) of the JSPS Japan. The numerical calculations were carried out on the TSUBAME2.5 supercomputer in the Tokyo Institute of Technology in research project (ID: hp170032).

References

1. Beugre, D., Calvo, S., Dethier, G., Crine, M., Toye, D., Marchot, P.: Lattice Boltzmann 3D flow simulations on a metallic foam. *J. Comput. Appl. Math.* **234**(7), 2128 – 2134 (2010)
2. Bouzidi, M., Firdaouss, M., Lallemand, P.: Momentum transfer of a boltzmann-lattice fluid with boundaries. *Phys. fluids* **13**(11), 3452–3459 (2001)
3. Box, G.E., Muller, M.E., et al.: A note on the generation of random normal deviates. *The annals of mathematical statistics* **29**(2), 610–611 (1958)
4. Busse, A., Lützner, M., Sandham, N.D.: Direct numerical simulation of turbulent flow over a rough surface based on a surface scan. *Computers & Fluids* **116**, 129–147 (2015)
5. Busse, A., Thakkar, M., Sandham, N.: Reynolds-number dependence of the near-wall flow over irregular rough surfaces. *J. Fluid Mech.* **810**, 196–224 (2017)
6. Chikatamarla, S., Frouzakis, C., Karlin, I., Tomboulides, A., Boulouchos, K.: Lattice Boltzmann method for direct numerical simulation of turbulent flows. *J. Fluid Mech.* **656**, 298–308 (2010)
7. Chukwudozie, C., Tyagi, M.: Pore scale inertial flow simulations in 3-D smooth and rough sphere packs using lattice Boltzmann method. *AIChE J.* **59**, 4858–4870 (2013)
8. Coleman, H., Hodge, B., Taylor, R.: A re-evaluation of schlichting’s surface roughness experiment. *ASME, Transactions, Journal of Fluids Engineering* **106**, 60–65 (1984)
9. d’Humières, D., Ginzburg, I., Krafczyk, M., Lallemand, P., Luo, L.S.: Multiple-relaxation-time lattice Boltzmann models in three dimensions. *Phil. Trans. R. Soc. A* **360**, 437–451 (2002)
10. Dirling JR, R.: A method for computing roughwall heat transfer rates on reentry nosetips. In: 8th Thermophysics Conference, p. 763 (1973)

11. Dupuis, A., Chopard, B.: Theory and applications of an alternative lattice boltzmann grid refinement algorithm. *Physical Review E* **67**(6), 066707 (2003)
12. Dvorak, F.: Calculation of turbulent boundary layers on rough surfaces in pressure gradient. *AIAA journal* **7**(9), 1752–1759 (1969)
13. Fattahi, E., Waluga, C., Wohlmuth, B., Rde, U., Manhart, M., Helmig, R.: Lattice boltzmann methods in porous media simulations: From laminar to turbulent flow. *Comput. Fluids* **140**, 247–259 (2016)
14. Flack, K.A., Schultz, M.P.: Review of hydraulic roughness scales in the fully rough regime. *J. Fluids Engng.* **132**(4), 041203 (2010)
15. Flack, K.A., Schultz, M.P., Barros, J.M., Kim, Y.C.: Skin-friction behavior in the transitionally-rough regime. *Int. J. Heat Fluid Flow* **61**, 21–30 (2016)
16. Fukagata, K., Iwamoto, K., Kasagi, N.: Contribution of reynolds stress distribution to the skin friction in wall-bounded flows. *Phys. Fluids* **14**(11), L73–L76 (2002)
17. Gehrke, M., Janßen, C., Rung, T.: Scrutinizing lattice boltzmann methods for direct numerical simulations of turbulent channel flows. *Comput. Fluids* **156**, 247–263 (2017)
18. Hasert, M., Bernsdorf, J., Roller, S.: Lattice Boltzmann simulation of non-Darcy flow in porous media. *Procedia Computer Science* **4**, 1048–1057 (2011)
19. Huang, C., Shi, B., He, N., Chai, Z.: Implementation of Multi-GPU based lattice Boltzmann method for flow through porous media. *Adv. Appl. Math. Mech.* pp. 1–12 (2015)
20. Iwamoto, K., Suzuki, Y., Kasagi, N.: Database of fully developed channel flow-thtlab internal report no. ILR-0201, Rapport technique, THTLAB, Dept. of Mech. Engng., The Univ. of Tokyo (2002)
21. Jin, Y., Uth, M., Herwig, H.: Structure of a turbulent flow through plane channels with smooth and rough walls: An analysis based on high resolution DNS results. *Comput. Fluids* **107**, 77 – 88 (2015)
22. Kang, S.K., Hassan, Y.A.: The effect of lattice models within the lattice Boltzmann method in the simulation of wall-bounded turbulent flows. *J. Comput. Phys.* **232**(1), 100 – 117 (2013)
23. Krogstad, P.Å., Antonia, R., Browne, L.: Comparison between rough-and smooth-wall turbulent boundary layers. *J. Fluid Mech.* **245**, 599–617 (1992)
24. Kuwata, Y., Suga, K.: Anomaly of the lattice boltzmann methods in three-dimensional cylindrical flows. *J. Comput. Phys.* **280**, 563 – 569 (2015)
25. Kuwata, Y., Suga, K.: Large eddy simulations of pore-scale turbulent flows in porous media by the lattice boltzmann method. *Int. J. Heat Fluid Flow* **55**, 143–157 (2015)
26. Kuwata, Y., Suga, K.: Imbalance-correction grid-refinement method for lattice Boltzmann flow simulations. *J. Comput. Phys.* **311**, 348–362 (2016)
27. Kuwata, Y., Suga, K.: Lattice boltzmann direct numerical simulation of interface turbulence over porous and rough walls. *Int. J. Heat Fluid Flow* **61**, 145–157 (2016)
28. Kuwata, Y., Suga, K.: Transport mechanism of interface turbulence over porous and rough walls. *Flow, Turb. Combust.* **97**(4), 1071–1093 (2016)
29. Lammers, P., Beronov, K.N., Volkert, R., Brenner, G., Durst, F.: Lattice BGK direct numerical simulation of fully developed turbulence in incompressible plane channel flow. *Comput. Fluids* **35**(10), 1137–1153 (2006)
30. Li, X., Zhang, Y., Wang, X., Ge, W.: GPU-based numerical simulation of multi-phase flow in porous media using multiple-relaxation-time lattice Boltzmann method. *Chem. Eng. Sci.* **102**, 209 – 219 (2013)
31. Musker, A.: Universal roughness functions for naturally-occurring surfaces. *Trans.the Canadian Soc. Mech. Engng.* **6**(1), 1–6 (1980)
32. Napoli, E., Armenio, V., De Marchis, M.: The effect of the slope of irregularly distributed roughness elements on turbulent wall-bounded flows. *J. Fluid Mech.* **613**, 385–394 (2008)
33. Nikuradse, J.: Laws of flow in rough pipes. In: *VDI Forschungsheft*. Citeseer (1933)
34. Parmigiani, A., Huber, C., Bachmann, O., Chopard, B.: Pore-scale mass and reactant transport in multiphase porous media flows. *J. Fluid Mech.* **686**, 40–76 (2011)
35. Schlichting, H., Gersten, K., Krause, E., Oertel, H., Mayes, K.: *Boundary-layer theory*, vol. 7. Springer (1960)
36. Schultz, M.P., Flack, K.: Outer layer similarity in fully rough turbulent boundary layers. *Exp. Fluids* **38**(3), 328–340 (2005)

37. Sigal, A., Danberg, J.E.: New correlation of roughness density effect on the turbulent boundary layer. *AIAA journal* **28**(3), 554–556 (1990)
38. Suga, K., Kuwata, Y., Takashima, K., Chikasue, R.: A D3Q27 multiple-relaxation-time lattice Boltzmann method for turbulent flows. *Comput. Math. Appl.* **69**(6), 518–529 (2015)
39. Suga, K., Nishio, Y.: Three dimensional microscopic flow simulation across the interface of a porous wall and clear fluid by the lattice Boltzmann method. *The Open Transp. Phenom. J.* **1**, 35–44 (2009)
40. Suga, K., Tanaka, T., Nishio, Y., Murata, M.: A boundary reconstruction scheme for lattice Boltzmann flow simulation in porous media. *Prog. Comput. Fluid Dyn.* **9**, 201–207 (2009)
41. Tóth, G., Jánosi, I.M.: Vorticity generation by rough walls in 2D decaying turbulence. *J. Stat. Phys.* **161**(6), 1508–1518 (2015)
42. Townsend, A.A.: *The structure of turbulent shear flow*. Cambridge university press (1980)
43. Townsin, R., Byrne, D., Svensen, T., Milne, A.: Estimating the technical and economic penalties of hull and propeller roughness. *Trans. SNAME* **89**, 295–318 (1981)
44. Van Rij, J.A., Belnap, B., Ligrani, P.: Analysis and experiments on three-dimensional, irregular surface roughness. *ASME, Trans. J. Fluids Engng.* **124**(3), 671–677 (2002)
45. Wang, P., Wang, L.P., Guo, Z.: Comparison of the lattice boltzmann equation and discrete unified gas-kinetic scheme methods for direct numerical simulation of decaying turbulent flows. *Phys. Rev. E* **94**(4), 043304 (2016)
46. White, A.T., Chong, C.K.: Rotational invariance in the three-dimensional lattice Boltzmann method is dependent on the choice of lattice. *J. Comput. Phys.* **230**(16), 6367 – 6378 (2011)